Journal of Nuclear Materials 538 (2020) 152223

Contents lists available at ScienceDirect

Journal of Nuclear Materials

journal homepage: www.elsevier.com/locate/jnucmat

Insight into interface cohesion and impurity-induced embrittlement in carbide dispersion strengthen tungsten from first principles

Xuebang Wu [a, *], Xu Zhang [a, b], Z.M. Xie [a], Xiangyan Li [a], C.R. Miranda [c], C.S. Liu [a, **]

[a] Key Laboratory of Materials Physics, Institute of Solid State Physics, Chinese Academy of Sciences, Hefei, 230031, PR China
[b] University of Science and Technology of China, Hefei, 230036, PR China
[c] Instituto de Física, Universidade de São Paulo, CP 66318, São Paulo, SP, 05315-970, Brazil

HIGHLIGHTS

- Coherent W (100)-TMC(100) interfaces have better stability than the semi-coherent W (110)-TMC(100) ones.
- The impurities H, He, N, O, S, and P tend to segregate to the interface and act as strong embrittlers.
- Interface provides a rapid channel to facilitate H and He transport along the interface.
- W-based materials with a multi-scale interface structure are suggested to enhance the overall performance.

ARTICLE INFO

Article history:
Received 2 October 2019
Received in revised form
9 March 2020
Accepted 4 May 2020
Available online 18 May 2020

Keywords:
Interfaces
Cohesion
Interfacial segregation
Tungsten
First-principles calculations

ABSTRACT

The fundamental understanding of interface properties is crucial in materials design and lifetime predictions. In this work, the stability, adhesion and impurity-induced embrittlement of interfaces between tungsten (W) and transition metal carbides (TMC = ZrC, TiC, TaC, HfC, MoC, and VC) have been investigated by first-principles calculations. For all the systems, the coherent W (100)-TMC(100) interfaces show better stability with lower interface energies than the semi-coherent W (110)-TMC(100) ones. The impurities hydrogen, helium, oxygen, and nitrogen tend to segregate to the coherent interfaces and act as strong embrittlers. Furthermore, the interface could provide a low-barrier channel to facilitate hydrogen and helium transport. The present work provides key mechanistic insights towards interpreting recent experimental studies of the interface structure and the hydrogen isotope retention in W–ZrC, W–TiC, and W–TaC materials under irradiation and guides the preparation of future W-based materials with good resistance to irradiation damage.

1. Introduction

Strengthening by adding a second phase or precipitation has been an important approach to improve the mechanical properties of metals [1]. The structure and energetics of the heterophase interface play a crucial role in the materials design and lifetime predictions [2]. On the one hand, the coherent/semi-coherent structure is favorable for increasing the interfacial bonding strength [2]. At the same time, the fine precipitates are used as pining particles which suppress grain growth. The presence of precipitates depends strongly on the interface energy [3]. The higher the interface energy, the lower the driving force for forming the interface, and so the easier the grain growth. On the other hand, the dispersed fine-grained materials have a high-density interface that could act as defect sinks and generally exhibit better resistance to irradiation damage [4]. A typical example of the precipitate strengthening is Fe by NaCl-type transition metal carbides/nitrides (TMX, TM = Mo, Nb, Ti, Zr, Hf, V, etc. and X = C, N) to improve the mechanical properties and resistance to the hydrogen embrittlement [2,3,5].

Recently, the metal tungsten (W) has received much attention as a primary candidate for plasma-facing materials (PFMs) in future fusion reactors due to its excellent physical properties such as high melting point and low sputtering [6,7]. To overcome the drawback of room-temperature brittleness of pure W, advanced nanostructured W alloys using oxide/carbide dispersion strengthening were developed, such as W–TiC, W–TaC, W–ZrC, and W–Y_2O_3

* Corresponding author.
** Corresponding author.
E-mail addresses: xbwu@issp.ac.cn (X. Wu), csliu@issp.ac.cn (C.S. Liu).

https://doi.org/10.1016/j.jnucmat.2020.152223
0022-3115/

alloys [8]. The prepared W−TiC and W−ZrC alloys show a high fracture strength at room-temperature, super-plasticity, and superior resistance to neutron irradiation and thermal heat load [9,10]. At a low flux of 10^{22} $m^{-2}s^{-1}$ and fluence of $4.5 \times 10^{26}m^{-2}$, the deuterium (D) retention in the W−TiC samples seem to be low compared with the retention in pure W [11], but at a high flux of $10^{23}m^{-2}s^{-1}$ and fluence of $10^{27}m^{-2}$, the D retention in W−TiC/TaC alloys are significantly higher compared to pure W at the low temperature [12]. From the selected area diffraction pattern and high-resolution transmission electron microscopy [9,13], the particle-matrix phase boundaries have coherent structure with W (110)||TiC(200) or W (110)||ZrC(200) orientation. This observation follows the Baker-Nutting (B−N) orientation relationship between bcc metals and NaCl-type carbides [5,14,15] rather than the reported Kurdjumov-Sachs (K−S) orientation relationship. On the other hand, during fusion service and manufacture, the impurities such as H, He, N, and O are easily segregated to interfaces, leading to the decrease of mechanical properties of materials [16,17]. Therefore, the understanding of interface stability and cohesion, as well as the interaction between interface and impurities, is crucial for the development of advanced W materials by interface design.

Regarding the interface of the metal-carbide nanocomposite, it is difficult by experimental methods to obtain the crucial information such as interface energy and the bonding and electronic structure around the interface, which determines the interface stability and strength. On the other hand, atomistic simulations can help to resolve the interface problem, and the most reliable means for theoretical studies of materials properties are first-principles calculations based on density functional theory (DFT) [1,18−21]. Previously, the interfaces between bcc Fe and NaCl-type precipitates have been extensively investigated by first-principles [3,5,15,22−25]. The coherent and semi-coherent interface energies were estimated between Fe and transition metal carbides. The Fe (100)−TiC(100) coherent interface was found to be more stable than the Fe (110)−TiC(100) semi-coherent structure with lower interface energy. However, for the interface between W and transition metal carbides, few studies were reported about up to now. It was found that the semi-coherent W (110)−TiC(100) interface is thermodynamically more stable with lower interface energy. Also, it shows higher interface strength than the coherent W (100)−TiC(100) interface [26]. Additionally, the W (110)−ZrC(111) interface is more favorable compared to others with a strong W−C bond [27]. Recent results show that the coherent ZrC(200)-W (100) interface has the highest interfacial stability with the lowest interface energy [28]. However, there is an ambiguity in the obtained interface energies because the strain energy due to a strong strain around the interface has not been taken into account. Furthermore, the assessment of interface on the hydrogen (H) and helium (He) retention in carbide doped W is still an open question, which is important to predict H recycling and retention under operational extreme conditions. Therefore, further work is needed to understand the relation between the interface and strain energies, the electronic structure, as well as the segregation properties of light impurities such as H and He to the interface.

To uncover the stable interface structure and its interaction with light element impurities, we performed first-principles calculations to study the properties of bcc W and transition metal carbides (TMC = ZrC, TiC, TaC, HfC, MoC, and VC) hetero-interfaces and trapping of interfaces to light element impurities (H, He, Li, Be, B, C, N, O, S, and P). First, we calculated the interface energies of coherent and semi-coherent interfaces to evaluate the stability of W-TMC interfaces. We also calculated the contribution of strain energies to the interface energies. Then, we performed the tensile test calculations to predict the mechanical tensile strength of the interfaces. Further, we investigated the segregation of light impurities to the coherent interfaces to predict the trapping effect of interfaces and examine the change of interface cohesion due to the presence of impurities. The electronic structures of the interfaces are also discussed. Finally, the interfacial structures, critical radius of carbide particles, and the H isotope retention of carbide doped W materials were considered with available experimental results. These results not only provide a consistent explanation for the recent experimental observations, but also propose guidelines for the interface design of W materials with advanced irradiation tolerance.

2. Computational methods

All numerical calculations were performed using density functional theory implemented in the Vienna ab-initio simulation package (VASP) code [29,30]. The interaction between ions and electrons was described by the projector augmented wave potential (PAW) method [31]. The exchange and correlation functions were taken in a form proposed by Perdew and Wang within the generalized gradient approximation (GGA) [32,33]. The plane wave cutoff and k-point density were both checked for convergence for each system to be within 0.001 eV per atom. The cutoff energy of 500 eV was used in all calculations. All atoms were relaxed by the conjugated gradient method until the forces on each of them are less than 0.001 eV/Å in our calculations.

The calculated lattice parameters of body-centered cubic (bcc) W and HfC, TaC, TiC, ZrC, MoC, and VC with NaCl structure are 3.177, 4.644, 4.478, 4.341, 4.728, 4.383, and 4.160 Å, respectively. These values are in good agreement with previous experimental and theoretical data [3,15,34,35]. It is generally expected that small carbides such as ZrC and TiC precipitates form a coherent interface with W. The coherent interface is the simplest ones to model. They are characterized by a perfect alignment of atomic planes across the interface, where the eventual lattice mismatch is accommodated by elastic expansion/compression of one or both phases. For the semi-coherent interface, the strain energy needed to make the interface coherent becomes very large, and it is more favorable to form an array of misfit dislocations to release the accumulated elastic stress. In the present study, we focused primarily on the Baker-Nutting orientation W (100)-TMC(100) and W (110)-TMC(100), for calculations of the coherent and semi-coherent interfaces between bcc W and transition metal carbides, as shown in Fig. 1.

For reliable results, the slab needs to be thick enough to resemble a bulk-like environment in the inner part. The convergence of results for different interfaces concerning their cell sizes is determined by comparing the site-projected density of states (DOS) of the interface and the bulk supercell. Thirteen layers of W (100) and W (110) and nine layers of TMC(100) were employed to establish the interface models. For the W (100)-TMC(100) coherent interface models, three kinds of interface boding states were considered, which are (i) “W-on-C” configuration, where the W atoms are on top of C atoms, (ii) “W-on-TM” configuration, and (iii) “bridge” configuration where the W atoms have two C atoms and two TM atoms as nearest neighbors. Each layer of W and TMC contains four W atoms, four TM atoms, and four C atoms. For these supercells, a $6 \times 6 \times 1$ k-point mesh was used for the Brillouin-zone integration. Interestingly, both the “W-on-TM” and “bridge” configurations were spontaneously changed into “W-on-C” configuration after complete relaxation (cell vectors and atomic positions), indicating the latter is more stable compared to others. For the W (110)-TMC(100) semi-coherent interface models, it is obtained by joining two-unit cells of W (110) and three-unit cells of TMC(100). Each layer of W and TMC contains four W atoms, three TM atoms, and three C atoms. The Brillouin zone integration was sampled on a $5 \times 15 \times 1$ k-point mesh.

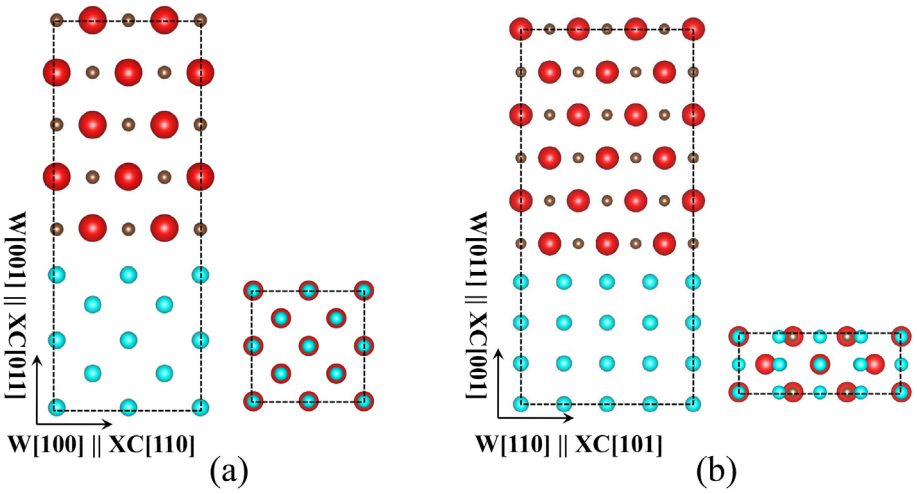

Fig. 1. Atomic structures of the two investigated interface models of (a) W (100)–ZrC(100) and (b) W (110)–ZrC(100) interfaces. The red, brown, cyan spheres represent Zr, C, and W atoms, respectively. (For interpretation of the references to colour in this figure legend, the reader is referred to the Web version of this article.)

3. Results

3.1. Interface energies

To characterize the stability of an interface, the interface energies were determined by subtracting the sum of the total energies of all the individual phases from the total energy of the system including the interface.

$$\gamma_{\text{int}} = \left[E_{PB} - E^{W}_{Bulk} - E^{TMC}_{Bulk}\right] \Big/ 2A, \tag{1}$$

where E_{PB} is the total energy of supercell containing the investigated interface configuration, while E^{W}_{Bulk} and E^{TMC}_{Bulk} are total energies of supercells containing the two bulk phases with the same numbers of atoms as the interface supercell, A is the interfacial area, and the factor 2 in the denominator takes into account that there are two equal interfaces in the supercell.

As described above, the bulk phases are usually strained to match at the interface as they generally have different lattice parameters. Consequently, the interface energy includes a contribution from stress due to the lattice mismatch between two sides of the interface [2,36]. This is not a useful definition as the interface energy now depends on how many strained layers of the bulk are retained in the calculations. The interface energy thus needs to be defined relative to the strained bulk (see Fig. 2). To quantify the strain contributions when calculating the interface energies, we subtract off the strain energy E_s by taking the total energy difference between the distorted supercells which have the lattice parameters taken from the corresponding interface models, and the fully relaxed bulk phases, which is defined as

$$E_s = \sum_{i=W,TMC} \left(E_{s,i} - N_i E_{i,bulk}\right), \tag{2}$$

where $E_{s,i}$ is the energy of strained supercell of phase i (W or TMC) which consists of the same atomic numbers and in-plane lattice parameters as that in the corresponding interface models but allowing the z-direction of the supercell to relax, $E_{i,\ bulk}$ is the energy per unit of the relaxed bulk phase i containing N_i units of phase i.

Fig. 3 shows the calculated interface energies between W and TMC of ZrC, TiC, TaC, HfC, MoC, and VC. The values of interface energies, strain energies, and the corresponding fixed and relaxed parameters on the xy interface plane are shown in Table 1. It can be seen from Table 1 that the strain energies are closely related to the distortion of interface plane between fixed and relaxed supercells for W and TMC phases. After subtracting off the contribution of strain energy, the interface energies of W (100)-TMC(100) coherent interfaces are found to be lower than those of semi-coherent W (110)-TMC(100) ones. This suggests that the W (100)-TMC(100) interfaces are thermodynamically favorable and therefore likely be formed in actual situations, which is consistent with the previous experimental observations of the coherent interfaces with orientations of W (100)–ZrC(100) and W (100)–TiC(100) [9,13]. Note that the negative γ values of the W (100)–TaC(100), W (100)–MoC(100), and W (100)–VC(100) interfaces indicate that the interdiffusion between W and TaC/MoC/VC may occur in the interface region. It is known that the low interface energy and equilibrium carbon concentration are effective in suppressing the coarsening of the second-phase during preparation [3]. So in the point of interface energies, the TaC, MoC, and VC precipitate are expected to be more favorable to control the size of precipitate within the W matrix. However, so far, no experimental results about the preparation of MoC and VC doped W materials were reported. Moreover, the interface energy of W (100)–ZrC(100) also has a low value of 0.31 J/m^2. This suggests that ZrC can be a useful precipitate to strengthen W.

Our present results of interface energies of W–ZrC and W–TiC alloys are significantly different from the previous findings [26,27]. This indicates the importance of strain energy to contribute to interface energy. Moreover, the structure of the interface slab, such as the thickness and vacuum layer, can also lead to distinct results. However, it is worth to say that the γ values of W (100)-TMC(100) interfaces are lower than those of W (110)-TMC(100) interfaces from both the methods. This indicates that W (100)-TMC(100) is rather stable and, therefore, likely to be observed in experimental studies. Those observations match well with the orientation of coherent W (100)–ZrC(100) and W (100)–TiC(100) interfaces from experimental results [9,13].

To gain insight into the stability of W-TMC interfaces, we also explore the electronic structure to examine the bonding properties. Due to the interfacial diffusion in some interfaces, the charge density difference was evaluated to the atomic electronic density, instead of the isolated slabs. Here the charge density difference $\Delta\rho$ of interfaces is defined by

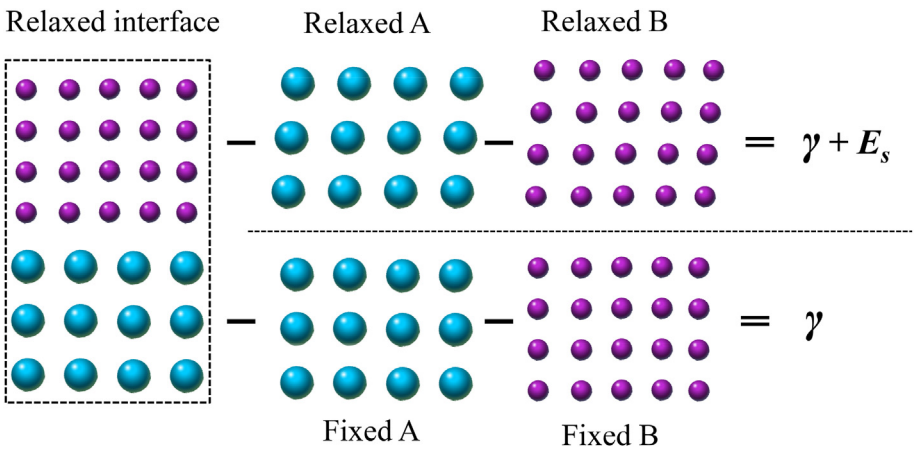

Fig. 2. (a) Sum of interface energy and strain energy by subtracting off total energies of relaxed A and B from that of the relaxed interface model; (b) interface energy by subtracting off total energies of strained A and B from that of relaxed interface model.

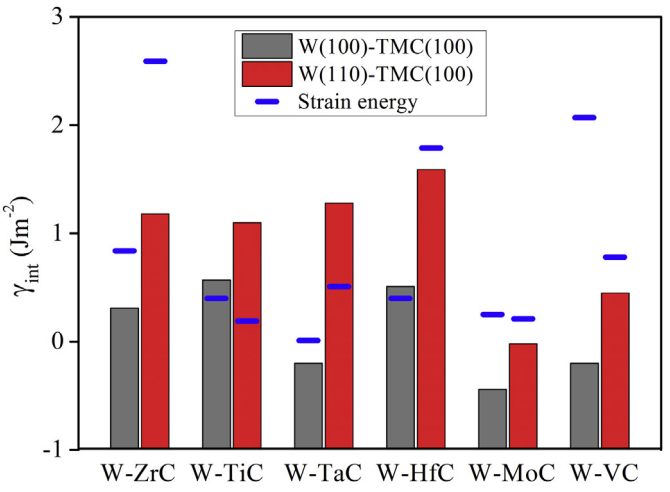

Fig. 3. Interface energies of W (100)-TMC(100) and W (110)-TMC(100) between W and NaCl-type carbides of ZrC, TiC, TaC, HfC, MoC and VC. Also included in the figure are the results of strain energies.

$$\Delta\rho = \rho_W + \rho_{TMC} - \rho_{PB}, \quad (3)$$

where ρ_{PB}, ρ_W, and ρ_{TMC} are the total charge density of the W-TMC interface, and pure W and ZrC after removing the ZrC and W layers, respectively. Negative values represent that local electrons are depleted, and positive values mean that local electrons are accumulated. Fig. 4 shows the $\Delta\rho$ distribution of atoms around the W-TMC interfaces. It is noticed that there is a substantial rearrangement of electrons around the interface from various $\Delta\rho$ values. For the W (100)-TMC(100) interfaces, we can find that significant charge accumulation occurs between interfacial C and W atoms, indicating that strong covalent bonds are formed in the interface. This results from the valence charge transfer from W to C atoms (based on the Bader Charge analysis) due to the higher electronegativity of C element than W. The interfacial separation distances of coherent interfaces are in the range of 2.05–2.10 Å, which is slightly larger than the shortest distance of 1.96 Å in a bulk W. For the W (100)–TaC(100), W (100)–MoC(100) and W (100)–VC(100) interfaces in Fig. 4(d)–(f), except the strong bonding between W and C atoms, the charges are delocalized and spread around the interfacial region. This may be the reason why the interface energies show negative values. For W (110)-TMC(100) interfaces in Fig. 4(g)–(i), the charge redistribution also mainly localized at the interface. After relaxation, two C atoms at the layer of ZrC diffuse toward the W layer, and the charge spread near the interface, suggesting the formation of strong bonding between the two slabs.

3.2. Tensile test calculations

A rigid type of tensile test calculations is performed to obtain the fracture energy E_{frac} and the tensile strength σ_{max} (maximum tensile stress), as presented in Ref. [37–39]. A fracture plane is chosen

Table 1
Interface energies γ_{int}, strain energies E_s, and the corresponding fixed and relaxed parameters ($\vec{a} \times \vec{b}$) of interface planes for coherent W (100)-TMC(100) and semi-coherent W (110)-TMC(100) interfaces.

System	$(\vec{a} \times \vec{b})_{fixed}$ (Å × Å)	$(\vec{a} \times \vec{b})_{relaxed}$-W slab (Å × Å)	$(\vec{a} \times \vec{b})_{relaxed}$-TMC slab (Å × Å)	$E_s^{(W)}$ (J m^{-2})	$E_s^{(TMC)}$ (J m^{-2})	γ_{int} (J m^{-2})
W (100-ZrC(100)	3.28 × 3.28	3.18 × 3.18	3.34 × 3.34	0.65	0.19	0.31
W (100)–TiC(100)	3.13 × 3.13	3.18 × 3.18	3.07 × 3.07	0.15	0.25	0.57
W (100)–TaC(100)	3.17 × 3.17	3.18 × 3.18	3.17 × 3.17	0.01	0	−0.20
W (100)–HfC(100)	3.25 × 3.25	3.18 × 3.18	3.28 × 3.28	0.31	0.09	0.51
W (100)–MoC(100)	3.13 × 3.13	3.18 × 3.18	3.10 × 3.10	0.17	0.08	−0.44
W (100)–VC(100)	3.07 × 3.07	3.18 × 3.18	2.93 × 2.93	0.98	1.09	−0.20
W (110)–ZrC(100)	9.51 × 3.25	8.97 × 3.19	10.03 × 3.34	1.45	1.14	1.18
W (110)–TiC(100)	9.08 × 3.13	8.97 × 3.19	9.20 × 3.07	0.11	0.08	1.10
W (110)–TaC(100)	9.23 × 3.17	8.97 × 3.19	9.50 × 3.16	0.25	0.26	1.28
W (110)–HfC(100)	9.43 × 3.22	8.97 × 3.19	9.85 × 3.28	0.96	0.83	1.59
W (110)–MoC(100)	9.08 × 3.13	8.97 × 3.19	9.30 × 3.10	0.08	0.13	−0.02
W (111)–VC(100)	8.92 × 3.08	8.97 × 3.19	8.79 × 2.93	0.44	0.34	0.45

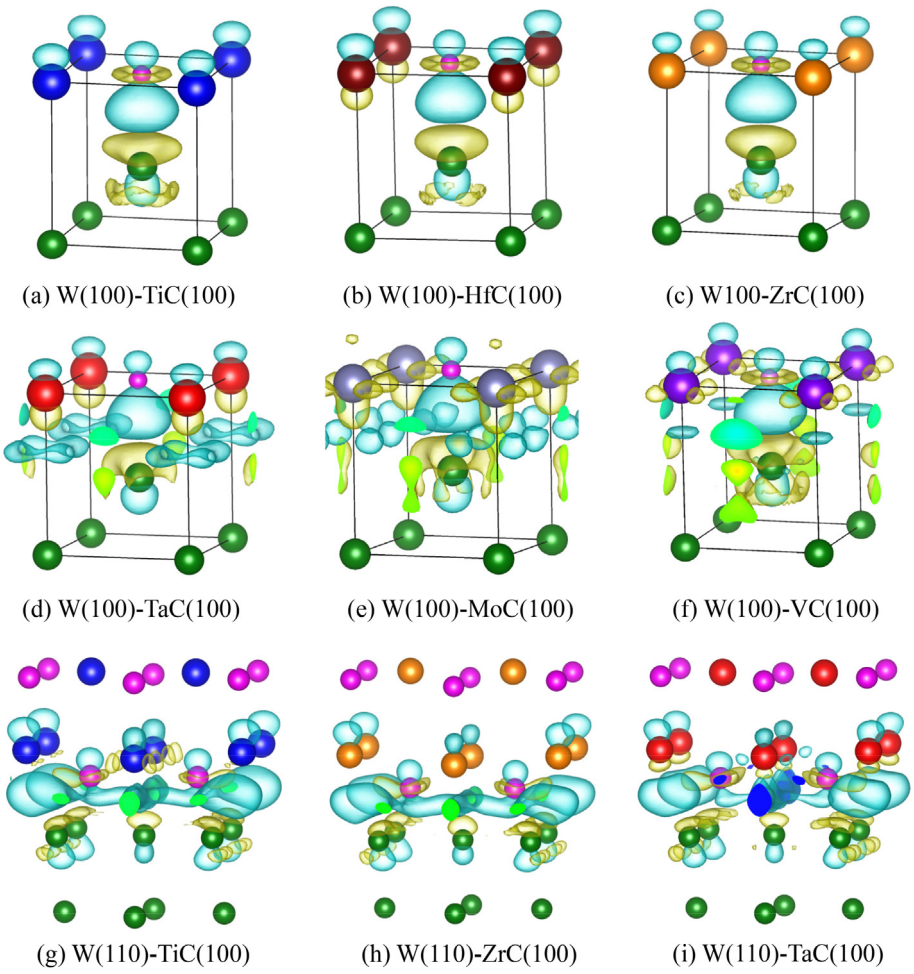

Fig. 4. Isosurface plots of the differences in electron density of different interfaces. Light (yellow) shading shows the regions of electron depletion and light (cyan) shading shows accumulation regions. The isovalue is 0.007 e/Å^3 for W (100)-TMC(100) and 0.008 e/Å^3 for W (110)-TMC(100). The lower part (olive spheres) and the upper part represent W and different transition metal carbide structure, respectively. (For interpretation of the references to colour in this figure legend, the reader is referred to the Web version of this article.)

that gives the minimum cohesive energy. Then the upper and lower crystal blocks are rigidly separated by distances varying from −0.1 to 0.6 nm. This calculation method is easy and convenient to obtain σ_{max} since it avoids complex structural relaxation calculations under a large strain and can calculate the different strains independently. The fracture energy, E_{frac}, can be obtained according to

$$E_{frac} = (E_{\propto} - E_0)\Big/2A, \tag{4}$$

where E_0 and E_{∞} are the total energy of GB without separation and that with a considerable separation distance, respectively. The total energy versus separation distance is fitted by a universal binding function proposed by Rose et al. [40].

$$f(x) = E_{frac} - E_{frac}\left(1+\frac{x}{\lambda}\right)e^{-x/\lambda}, \tag{5}$$

where λ is the Thomas-Fermi screening length. The tensile stress is the derivative of $f(x)$:

$$f'(x) = E_{frac}xe^{-x/\lambda}\Big/\lambda^2. \tag{6}$$

The maximum of $f'(x)$ at $x=\lambda$ and corresponds to the maximum tensile strength σmax, therefore

$$\sigma_{\max} = f'(\lambda) = E_{frac}\Big/\lambda e. \tag{7}$$

Fig. 5(a) shows the calculated separation energies of the typical stable W (100)–TaC(100), W (100)–VC(100), and W (100)–ZrC(100) interfaces, as well as their Rose fitted curves. The obtained values of fracture energies for different W (100)-TMC(100) interfaces are summarized in Table 2. From Table 2, the E_{frac} values for W (100)–TaC(100) and W (100)–MoC(100) interfaces are higher than those of W (100)–ZrC(100), W (100)–TiC(100), and W (100)–HfC(100) interfaces, indicating the adhesion of the former interfaces are stronger. Fig. 5(b) shows the tensile stress as a function of the separation distance. For all the interfaces, the stress increases with increasing separation distance to reach the maximum tensile stress σ_{max} and then drops to reach zero. The values of σ_{max} for different coherent interfaces were also included in Table 2. Similarly, the W (100)–TaC(100) and W (100)–MoC(100) interfaces show a relatively higher σ_{max} than others.

3.3. Trapping of light elements at interfaces

The properties of irradiation resistance of carbide dispersion strengthening W materials are also significant for their application as PFM in future fusion devices, especially the accumulation of H and He under plasma. Previous experimental studies have focused

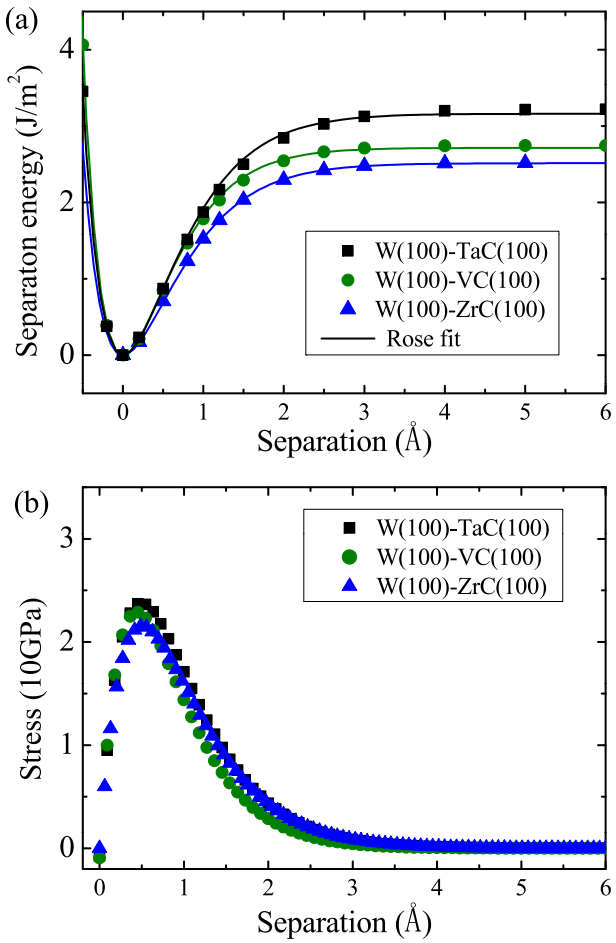

Fig. 5. (a) Separation energy and (b) tensile stress vs. separation distance of the typical coherent interfaces W (100)–TaC(100), W (100)–VC(100), W (100)–ZrC(100) interfaces. The solid lines in Fig. 6a denote the fit curves by the Rose function.

on the deuterium retention in ZrC, TiC and TaC doped W [12,41–43]. However, the underlying mechanism of the interface as trapping sites is still an open question. So the segregation and cohesion behaviors of light element impurities such as H, He, Li, Be, B, C, N, O, S and P in typical coherent W (100)–ZrC(100) and W (100)–TiC(100) interfaces were then considered.

To show how energetically an alloying atom tends to move to the interface from the bulk phase, the segregation energy E_{seg} of a light element atom X at the interface can be defined by

$$E_{seg} = E^X_{PB} - E_{PB} - \left(E^X_{Bulk} - E_{Bulk}\right), \tag{8}$$

where E^X_{PB} and E_{PB} are the total energies of the interface with and without the atom X, respectively, while E^X_{Bulk} and E_{Bulk} are the total energies of a bulk W supercell with and without X, respectively. Based on this definition, negative values of E_{seg} indicate that the considered site is energetically more favorable for the atom X than the stable site in bulk W. Then the energy needed for the atom X from the interface escape to bulk W is defined by Ref. [5],

$$E_{esc} = E_{seg} + E_{mig} + \Delta E_f, \tag{9}$$

where E_{mig} and ΔE_f are the migration energy barrier for the X atom in bulk W and the difference of solution energy between W and TMC, respectively. To obtain the most stable site of light element near the interface, a number of possible high-symmetry interstitial positions near the interface were optimized. Fig. 6 shows the initial and final positions after relaxation for the light elements. Surprisingly, after structural optimization, almost all of the impurities are not located in the interface region between the two crystals. But instead at the W place closest to the interface, as shown in Fig. 6(b). Note that most of the stable sites have similar symmetries as octahedral or tetrahedral sites in bulk W. For instance, H and He likes to stay near the tetrahedral site. At ehe same time, the impurities B, Be, C, N, O, P, S located at the octahedral site. Only Li tends to stay at the bridge site between two W atoms.

The segregation energies for different impurities to the W (100)–ZrC(100) and W (100)–TiC(100) interfaces, calculated according to Eq. (8), are shown in Fig. 7. Also included in the figure are the segregation energies of a typical grain boundary of W Σ3 (111) for comparison. For all the impurities, the segregation energies are negative, implying that they tend to segregate to the interface from the bulk W. Generally, the variation trend of the segregation energies is similar for all the interfaces and grain boundaries. The impurities Li, P, and S have a strong tendency to move towards the interface from the bulk environment. Note that for He, Li, Be, B, P, and S, the segregation energies to the interface are higher than those to the GB, which indicates that these impurities prefer to stay at the GB rather than the interface. For H, the segregation energies to W (100)–ZrC(100) and W (100)–TiC(100) are −0.93 eV and −0.88 eV, respectively, which are almost the same with that (−0.90 eV) to W Σ3 (111) GB. While for He, they are −2.19 eV and −2.42 eV, respectively, which are higher than that (−3.35 eV) to the GB.

A small amount of impurities into GBs or interfaces can significantly modify the mechanical properties such as strength and ductility of material. So the fracture energy of the W (100)–ZrC(100) interface, which could provide qualitative information on the impurity effect on the interface cohesion, were calculated from the difference between the two total energies according to

$$E_{frac} = \frac{E_\infty - E_0}{2A}, \tag{10}$$

where E_0 is the energy of interface without separation, and E_∞ is the energy when the separation distance is so considerable that the energy does not change any more. Fig. 8 shows the fracture energies of the W (100)–ZrC(100) interface doped with different impurities. For all the impurities, the fracture energies were lower than that of the pure interface, indicating that all impurities

Table 2
Properties of fracture energetic from theoretical tensile test calculations.

System	Fracture energy (J m^{-2})	tensile strength (GPa)	Critical separation (Å)
W (100)–ZrC(100)	2.51	18.94	0.49
W (100)–TiC(100)	2.50	20.52	0.44
W (100)–TaC(100)	3.16	23.71	0.49
W (100)–MoC(100)	3.13	24.55	0.47
W (100)–VC(100)	2.72	22.88	0.43
W (100)–HfC(100)	2.49	19.64	0.46

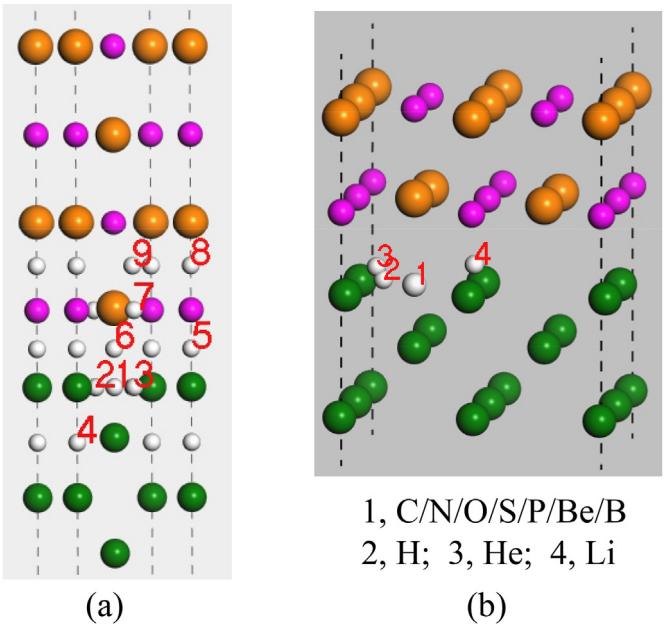

Fig. 6. (a) Initial possible positions and (b) the final stable positions for the light elements segregated at the W (100)–ZrC(100) interface The olive, orange, magenta, and white spheres represent W, Zr, C, and light element atoms, respectively. The stable position of C, N, O, S, P, Be, and B is the octahedral site at site 1, and H/He prefers to stay at the tetrahedral-like site 2 or 3, while Li prefers to stay at site 4. (For interpretation of the references to colour in this figure legend, the reader is referred to the Web version of this article.)

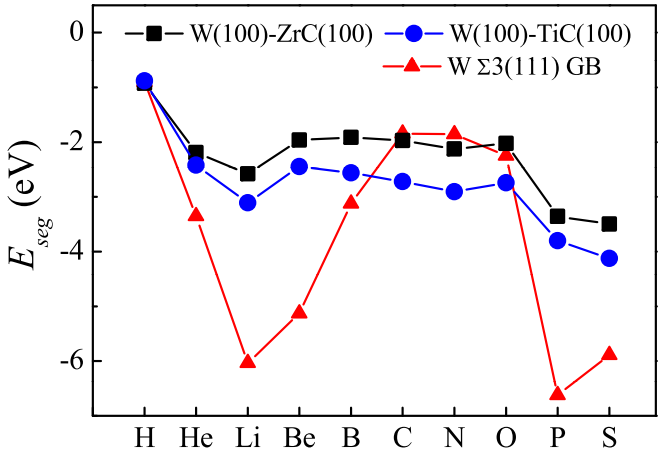

Fig. 7. Segregation energies of the light elements H, He, Li, Be, B, C, N, O, P, and S to the coherent interfaces W (100)–ZrC(100), W (100)–TiC(100), and the grain boundary of W Σ3 (111)[100].

segregated to the interface decrease the cohesion of the system. Note that the impurities He, Li, O, P, and S decrease the fracture energy the most, implying they are strong embrittler to the cohesion. To learn more about the origin, the bond length of W–C near the interface, marked by the line in Fig. 9, is shown in Fig. 8. Compared to the fracture energies, these two change tendencies are contrary across the series. As described above, the strong W–C bond plays an essential role in the stability and cohesion of the interface. The increase of the W–C bond length would decrease the cohesion of the interface.

As described above, charge density plays an important role in the analysis of interatomic bonding, as the charge accumulation/

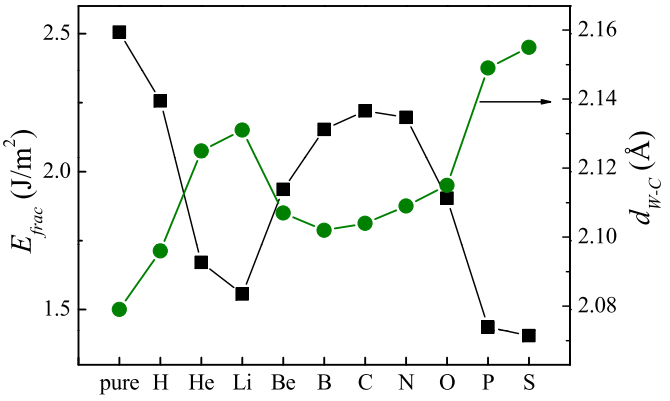

Fig. 8. Fracture energies of the pure W (100)–ZrC(100) interface and interfaces with segregated light element H, He, Li, Be, B, C, N, O, P and S, and the bond length between interfacial W and C (lines in Fig. 10a).

depletion can be a direct indicator of the strengthening/weakening of the chemical bond. Fig. 9 shows the charge density of pure W (100)–ZrC(100) interface and the interfaces doped with typical impurities H, Li, and S. As seen in Fig. 9(a), the interfacial W and C form a strong covalent bond after structure relaxation, which holds the two grains together and contributes most to the interface strength. In Fig. 9(b), the segregation of the H atom at the interface leads to a rearrangement of the charge density distribution. Comparing Fig. 9(a) and (b), there is a slight decrease of charge accumulation between W and C when H is inserted. So the W–C bond is weaker than that in the clean interface. When Li segregated at the interface in Fig. 9(c), it makes a strong distortion of the nearby structure. The W–C bond is elongated, and this is the probable origin of the much decease strength compared to the clean interface. For S segregated interface in Fig. 9(d), the W–C bond is even more decreased, because considerable charge transfers to the S atom due to its large electronegativity. This may be the reason why S is a strong embrittler at the interface.

To further analyze the bonding characteristics of the W (100)–ZrC(100) interface with impurities, the site-projected DOSs have been performed and shown in Fig. 10. As for the perfect coherent interface in Fig. 10(a), as described above, the adhesion strength and stability of interface primarily depend on the hybridizations among Zr 4*d*, W 5*d*, and C 2*p* states, forming a strong covalent bonding. For H segregated to the interface in Fig. 10(b), there is no noticeable change of interfacial atoms in the DOS compared to that of the pure interface, but a small hybridization peak appears at −8.0 eV between H 2*s* and W 5*d* states. So, the occupied states of interfacial W, Zr, and C atoms were depleted, weakening the interfacial strength. As for the interface with a Li atom in Fig. 10(c), the *s* state of Li becomes non-localized and more dispersed, and the significant distortion around Li should be the main reason why Li acts as a strong embrittler to the interface cohesion. As for the interface with an S atom in Fig. 10(d), the S 2*s* and 2*p*, W 5*d*, Zr 4*d*, and C 2*p* states exhibit a new narrow sharp peak at −16.2 eV and a broad peak between −8.6 eV and −6.6 eV. The hybridization between S 2*s* and W 5*d* leads to the strong depletion of occupied states between interfacial W 5*d*, Zr 4*d*, and C 2*p*, causing the substantial weakening of interface strength, which is in a good agreement with the charge density result in Fig. 9(d).

Not only the perfect interface has been considered, but we also calculated the trapping properties of vacancies at the coherent W (100)–ZrC(100) interface. Transition metal carbides including ZrC, are known to exhibit significant stoichiometric variations of the carbon sublattice, with the amount of C vacancies reaching up to

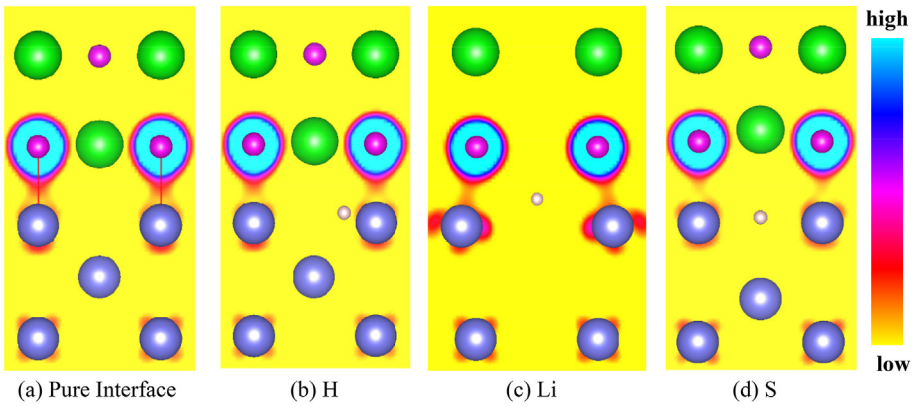

Fig. 9. Charge density for the pure W (100)–ZrC(100) interface and typical interfaces with segregated H, Li, and S (isovalue is 0.083 e/Å^3).

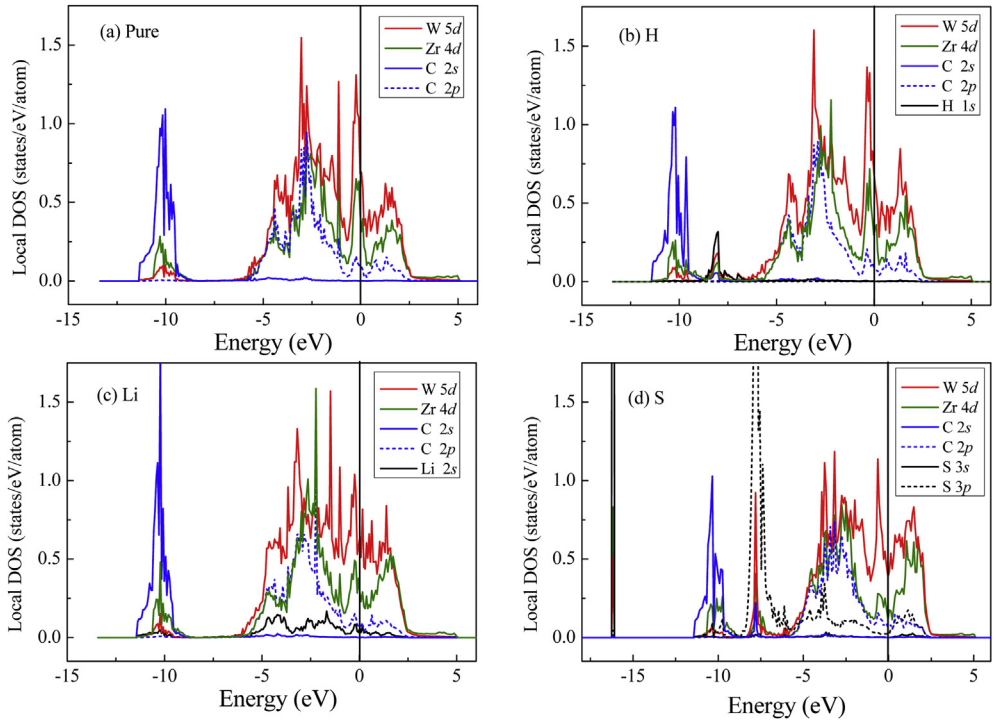

Fig. 10. Site-projected DOS of the W, Zr, C, and typically segregated impurities H, Li and S atoms located at the W (100)–ZrC(100) interface. The line at the zero-energy point denotes the Fermi level.

50% [5,44]. Besides, the vacancies near the interface may be easily formed during the H/He plasma irradiation under a fusion environment. Such vacancies near the interface can facilitate H and He trapping and diffusion. For the coherent interface, nine different vacancy locations (V1–V6), including C, Zr, and W vacancies, were investigated, as illustrated in Fig. 11. The vacancy formation energies were calculated according to

$$E_f(X) = E_{PB}^{Vac(X)} - E_{PB} + E(X), \tag{11}$$

where $E_{PB}^{Vac(X)}$ is the energy of the interface with a vacancy and $E(X)$ is the energy per atom in the bulk X phase. Here E (Zr) is the energy per Zr atom in the hexagonal close-packed bulk Zr and calculated to be −8.40 eV, and E(C) is the energy per C atom in the graphite solid and calculated to be −8.01 eV. The values of vacancy formation energies at different positions are listed in Table 3. For comparison, the results obtained for vacancies in bulk ZrC and W were also included. For a C vacancy, the formation energy of V1 is slightly higher than that in bulk ZrC, while those of V2 and V3 are lower. For a Zr vacancy, all the formation energies are lower than that in bulk ZrC. For a W vacancy, the formation energy of V4 is found to be lower than that in bulk W, while those of V5 and V6 are higher. Note that the formation energies of the C vacancy are lower than others, suggesting it will preferentially be formed under a specific condition such as high energy plasma irradiation. The binding energy of a vacancy with H or He near the interface was calculated as follows,

$$E_b^{Vac-X} = E_{PB}^{Vac} + E_{PB}^{X} - \left(E_{PB}^{Vac+X} + E_{PB}\right), \tag{12}$$

where E_{PB}^{Vac} and E_{PB}^{Vac+X} are total energies of the interface with a vacancy and that containing both a vacancy and an atom X, respectively. Here for the interface with a C vacancy (V1–V3), the H

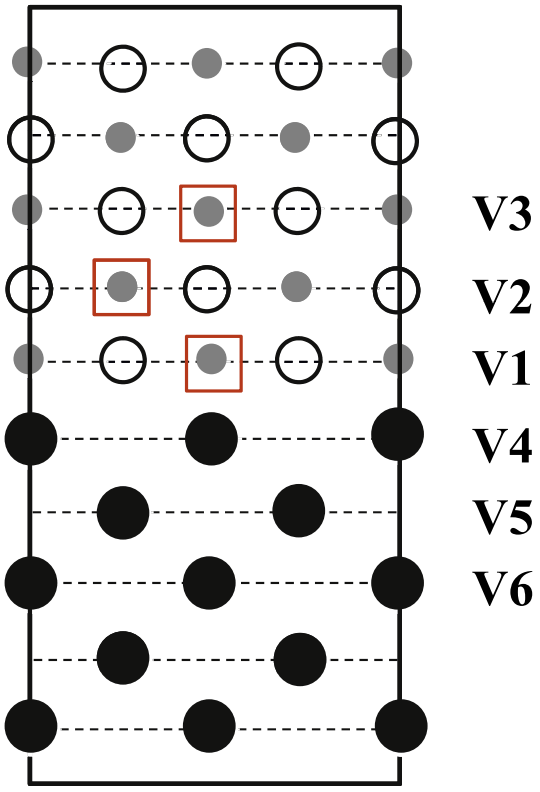

Fig. 11. Illustration of the different C vacancies positions in the vicinity of the W (100)–ZrC(100) interface. V1–V3 denote the C or Zr vacancy, while V4–V6 denote the W vacancy.

Table 3
Characteristic vacancy formation energy E_f, segregation energy E_{seg} of H and He at the vacancy and binding energy E_b between H/He and vacancy in W (100)–ZrC(100) interfaces and the bulk materials.

Energy (eV)	V1	V2	V3	Bulk
E_f(C)	2.54	2.03	2.03	2.34
E_f (Zr)	6.37	8.24	8.83	8.93
E_f(W)	2.83 (V4)	3.64 (V5)	3.45 (V6)	3.21
E_{seg}(H)	−1.57	−1.58	−1.60	/
E_{seg} (He)	−1.60	−1.77	−1.89	/
E_b (Vac-H)	0.92	0.93	0.95	1.19
E_b (Vac-He)	1.46	1.63	1.75	4.55

or He atom prefers to stay at the center of the vacancy. For comparison, the binding energy of a vacancy with H or He in a bulk W was calculated by

$$E_b^{Vac-X}(Bulk) = E_{Bulk}^{Vac} + E_{Bulk}^{X} - \left(E_{Bulk}^{Vac+X} + E_{Bulk}\right), \quad (13)$$

where E_{Bulk}^{X} is the total energy of the system with an H or He atom at a tetrahedral interstitial site in W. E_{Bulk}^{Vac+X} is the total energy of the system with an H or He atom in a W vacancy, where H likes to occupy close to the octahedral interstitial site next to the vacancy, and He prefers to stay at the center of the vacancy. The obtained values of binding energies of a vacancy with H and He at the interface and in a bulk W are presented in Table 3. It can be found that the binding energies at the interface are generally lower than those in bulk W. Also, the segregation energies of H and He to the C vacancy at the interface were calculated according to

$$E_{seg} = E_{PB}^{Vac+X} - E_{PB}^{Vac} - \left(E_{Bulk}^{X} - E_{Bulk}\right), \quad (14)$$

where E_{Bulk}^{X} and E_{Bulk} are the total energies of ZrC supercells with and without an interstitial X atom. In bulk ZrC, an interstitial H atom is stable on the tetrahedral site surrounding one C atom and three Zr atoms. Meanwhile, He is stable on the cube center site surrounding four Zr atoms and four C atoms, which are in good agreement with previous results [45–47]. The segregation energies of H and He to the vacancy at the interface are also listed in Table 3. It was found that the segregation energies of H are lower than that to the pure interface (−0.93 eV), while those of He are higher than that to the pure interface (−2.19 eV).

4. Discussion

4.1. Interface structures and critical radius

For the W-TMC interface structures, previous experimental results on W–TiC based materials show that it has a coherent interface that follows the Kurdjumov-Sachs (K–S) orientation relationship [13]. Recently, the observation of the microstructure of the W–ZrC material reveals that it has a coherent structure with a lattice match of $d_{(110)W} = 0.220$ nm ≈ $d_{(200)ZrC} = 0.231$ nm [9], as presented in Fig. 12(a). This coherent structure is responsible for increasing the interface cohesion that leads to the excellent mechanical properties and better resistance to thermal shock of this material. Compared with Fig. 12(a) and (b), the experimentally observed structure, such as the d-spacing of ZrC(200) and W (110), agrees well with the stable theoretical model of the W (100)–ZrC(100) coherent interface. So the previous coherent interface between W and TiC/ZrC follows the Baker-Nutting orientation relationship. It should be noted that the experimental observation is from the top view during the ion thinning process, and the ZrC particle is gradually come out surrounding the W matrix, as shown in the inset of Fig. 12(a). The well-separated interface of W (100)–ZrC(100) from the side view in Fig. 12(c) is the most stable because of the strong covalent bonding between W and C atoms. Due to the stability, this kind of interface will likely be the predominant type between the W matrix and the small ZrC particles.

Importantly, there is a critical radius r_c of a precipitate particle that can no longer be sheared through by dislocations, which is defined as [48].

$$r_c = \alpha \frac{Gb^2}{\gamma_{int}}, \quad (15)$$

where α is on the order of unity. Applying this concept to the W-TMC alloys, where $G = 161$ GPa, $b = 0.274$ nm (Burgers vector for bcc W) [49] and the different γ_{int}, resulting in a critical diameter of about 40 nm for W (100)–ZrC(100) coherent interface, and about 20 nm for W (100)–TiC(100) and W (100)–HfC(100) interfaces. Therefore, the yield point of W by adding second phase strengthening could be effectively increased below 40 nm for W–ZrC alloy and below 20 nm for W–TiC and W-HfC alloys. The larger-sized precipitate can be considered non-shearable. If such large particles reside in the W matrix, dislocation loops will accumulate around these particles, and this is a classical Orowan strengthening mechanism, which has a minimal effect on increasing the yield point. However, it dramatically enhances strain hardening through dislocation accumulation. In other words, if one wants to strongly improve the yield point of W alloys such as W–ZrC, the size of dispersed ZrC particles should be decreased to about 40 nm.

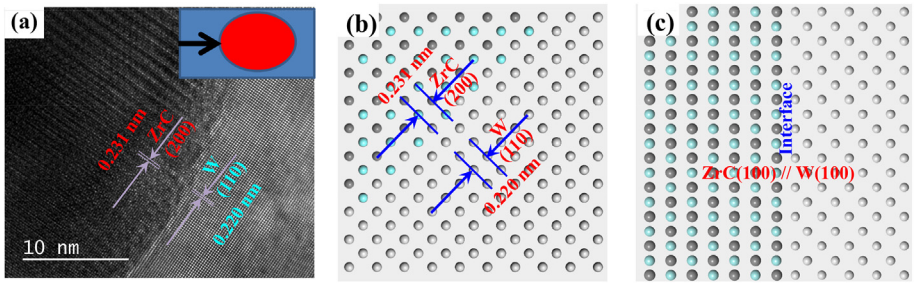

Fig. 12. Comparison with the experimental image with the relaxed simulation model for the coherent W–ZrC interface. (a) High-resolution transmission electron microscopy image of the coherent structure between W matrix and ZrC phase as viewed along [001]. (b) and (c) are the stable configurations for the coherent W (100)–ZrC(100) interface models as viewed along [001] (from the top) and [100] (from the side), respectively.

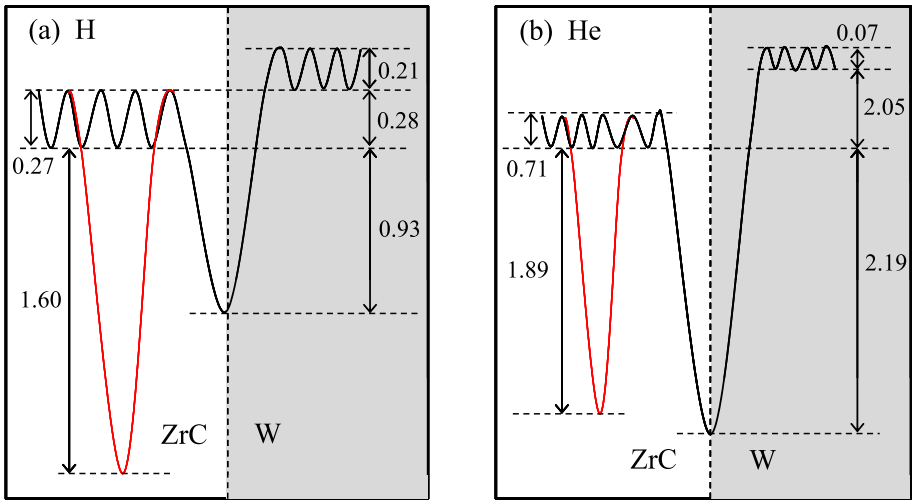

Fig. 13. Energy profile experienced by (a) H and (b) He at the coherent W (100)–ZrC(100) interface. The red curve denotes the interface with a C vacancy at the interface. (For interpretation of the references to colour in this figure legend, the reader is referred to the Web version of this article.)

4.2. Comparison with experiments and opportunities to advanced W materials

To characterize the H and He trapping properties of ZrC precipitate in W, we considered both the interface and the bulk-like region of the precipitate. Based on the above results, using similar methods in Ref. [5], it is possible to construct the energy profiles experienced by H and He around the interface, as shown in Fig. 13. The migration energy barriers of H and He in bulk W, bulk ZrC and W (100)–ZrC(100) coherent interface were investigated and summarized in Table 4. The energy barriers of H and He in pure W agree well with the previous calculation results [50,51]. The barrier of He in ZrC matches well with others [46,47], while that of H is different from the other [45] due to the different diffusion paths.

Fig. 13 shows the H and He energy profiles across the coherent interface (black line) and that in the presence of a C vacancy (red line). As for H in Fig. 13(a), the segregation energy at the C vacancy is lower than that at the pure interface, while for He in Fig. 13(b), the value at the C vacancy is higher than that at the pure interface. According to Eq. (9), the escape energies of H diffusion from the interface and the C vacancy to the nearest bulk interstitial site in W are 1.42 eV and 2.09 eV, respectively. And those of He from the interface and the C vacancy to bulk W are 4.31 eV and 4.01 eV, respectively. From Fig. 13, it is noted that the differences in formation energies of H and He in bulk W and ZrC are 0.28 eV and 2.05 eV, respectively. Therefore, the C vacancy presents a deep trap for H, while both the interface and C vacancy act as strong traps for He. This theoretical prediction agrees well with the recent experimental results that the C vacancy provides a strong trap for H in the iron/VC interface [52,53].

Recently, few available experimental data were obtained using the thermal desorption spectroscopy for carbide doped W–ZrC, W–TiC, and W–TaC materials [12,41–43]. Although the effective values of desorption activation energy were not given, which corresponds to the trap escape energy, the present results could provide a qualitative explanation for the experimental results. After the D plasma irradiation, Liu et al. found that the hydrogen retention in W–ZrC is much lower than that in pure W [43]. Moreover, the blister sizes of W–ZrC, W–TiC, and W-HfC are much smaller than that in pure W, which is similar to the previous results that no blister on W–TiC and W–TaC materials exposed at about 1050 K compared to pure W [12]. As mentioned above, the segregation energy of H to the interface is almost the same with that to grain

Table 4
Migration energy barrier of H and He in bulk W and carbides as well as the interfaces.

Materials	E^{H}_{mig} (eV)	E^{He}_{mig} (eV)
W	0.21	0.07
ZrC	0.27	0.71
TiC	0.27	0.35
W (100)–ZrC(100)	0.31	0.33
W (100)–TiC(100)	0.04	0.23

boundary in pure W. The interfaces provide additional sites for H bubble nucleation besides grain boundaries. The nano-carbide will disperse large bubbles into even small size, and consequently, many tiny H bubbles would be formed instead of large bubbles [54,55]. This may explain why the blister sizes of carbide dispersed W are much smaller than that in pure W. In addition, the enhanced irradiation resistance for carbide W may be caused by the grain boundary strengthening due to the presence of carbide precipitates [12,17,56,57]. The TMC precipitation and segregation of TMC constituents at grain boundaries lead to the grain boundary strengthening [12,17,56].

Moreover, the presence of TMC dispersoids will refine the grain size and so enhance the yield strength [57]. From Table 4, it can be found that the migration energy barriers of H and He along the W-TMC interfaces are less than 0.35 eV. Therefore, the interfaces could provide fast migration channels for H and He. It is anticipated that for tungsten materials with a columnar grain structure, H and He may diffuse out through the channels of grain boundaries or interfaces, as shown in Fig. 14(a). However, this speculation should be validated using mesoscopic approaches such as Kinetic Monte Carlo simulations to capture the H trapping, diffusivity, and concentration as well as dedicated experiments.

As for the H retention of W−TiC and W−TaC materials after the exposure at about 800 K and the high flux plasma exposure, the D concentrations were more than one order of magnitude higher compared to that in pure polycrystalline W, and a much higher D retention was found compared to those after the low-flux plasma exposure [12]. This is understandable because, under the high flux, the D retention is dominated by the trapping on the irradiation-induced defects such as vacancies. A higher flux leads to high irradiation defects as trapping sites for D. At high temperatures, H and He can diffuse towards the carbide precipitate and are trapped by the lattice defects such as C vacancies [45,46]. It is very difficult for H to migrate to the bulk W due to the high detrapping energy of 1.87 eV once they are trapped by C vacancies, as seen in Fig. 13(a). So the D trapping at the interface and the C vacancy becomes dominant at high temperatures.

As discussed above, the problem of H isotope retention in carbide doped W materials seems unfavorable for applications as PFMs in a fusion device. So it is necessary to reduce the H retention as much as possible. According to the present simulation, one possible way is to allow H to escape through the channels of interfaces and grain boundaries. So it is suggested that the multi-scale interface structure may be a good choice to enhance the overall performance of W-based materials synergistically, including micron-scale columnar parent grains, submicron ultrafine equiaxed subgrains, and nano-scale dispersion strengthened particle/matrix phase boundary interfaces, as shown in Fig. 14(b). Compared to nanocrystalline and ultra-fine-grained W, the micro-sized columnar grains not only reduce the scattering of hydrogen isotope but also they act as channels for H to diffuse along the columnar grain boundaries, thus decreasing the H retention in these materials. At the same time, the micron-sized grains could also improve the thermal conductivity of the material and thereby enhances its resistance to a high heat load. The submicron subgrains and nano-scale dispersion strengthened particle interfaces not only improve the strength/ductility of the materials but also act as sinks to capture the irradiation defects and suppress the formation of H/He bubbles and voids, improving the irradiation tolerance. However, as mentioned by Zibrov et al. [12], before making a plausible judgment of such materials for fusion application, the assessment of overall performance in a service environment such as the synergy of the presence of neutron irradiation damage and high-flux plasma exposure at high temperatures should be made.

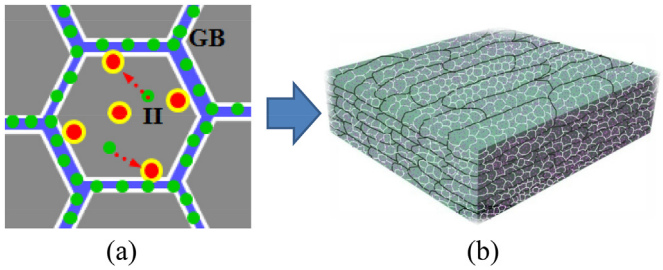

Fig. 14. Schematics of (a) the diffusion path for the H atom along the interface and grain boundary and (b) a possible multi-scale interfacial microstructure for future W materials with advanced properties.

5. Conclusion

In this work, the stability of the interfaces between tungsten and transition metal carbides (TMC = ZrC, TiC, TaC, HfC, MoC, and VC) and their trapping to light element impurities (H, He, Li, Be, B, C, N, O, S and P) have been investigated in detail. The calculated results can be summarized as follows.

(i) The contribution of strain energy to the interface energy cannot be ignored. After excluding the strain energy, the coherent W (100)-TMC(100) interfaces are more stable with lower interface energies than the semi-coherent W (110)-TMC(100) interfaces. The electronic structure analysis shows that there is a strong covalent bonding between the interfacial W and C atoms. The stable W (100)−ZrC(100) coherent interface matches well with the experimental images of the interface structures.

(ii) Based on the interface energies, it is estimated that for the W−ZrC alloys, the size of ZrC particles should be decreased to about 40 nm to improve the yield point of the materials, while smaller particles within 20 nm for W−TiC and W-HfC alloys.

(iii) The tensile test calculations of different coherent interfaces exhibit that the W (100)−TaC(100) and W (100)−MoC(100) interfaces have a relative higher fracture energy and tensile strength, indicating a higher interface adhesion.

(iv) Both the interface and the C vacancy in the carbide acts as strong traps to light element impurities such as H and He. At the same time, the segregation of light elements to the interface would decrease the cohesion of the system. The detrapping energies for H and He out of the interface are 1.14 eV and 2.26 eV, respectively. The migration energy barrier of H along the W−ZrC and W−TiC interfaces are 0.31 eV, and 0.04 eV, respectively. So the interfaces could provide a rapid diffusion path for H once it is trapped.

The present work not only provides a consistent explanation for recent experimental results about the H isotope retention in carbide doped tungsten, but also opens up additional avenues for future experimental preparation of advanced W materials. A multi-scale interface structure, including a micron-scale columnar parent grain, submicron ultrafine equiaxed subgrain, and nano-scale carbide/W interface, is suggested to synergistically improve the overall performance of W-based materials such as the mechanical properties, thermal conductivity, H retention, and irradiation tolerance.

CRediT authorship contribution statement

Xuebang Wu: Conceptualization, Investigation, Writing -

original draft, Writing - review & editing, Funding acquisition. **Xu Zhang:** Investigation, Formal analysis, Methodology. **Z.M. Xie:** Formal analysis, Writing - review & editing. **Xiangyan Li:** Investigation, Methodology, Writing - review & editing. **C.R. Miranda:** Writing - review & editing, Funding acquisition. **C.S. Liu:** Supervision, Funding acquisition.

Declaration of competing interest

The authors declare that they have no known competing financial interests or personal relationships that could have appeared to influence the work reported in this paper.

Acknowledgments

This work is supported by the National Key Research and Development Program of China (Grant No.: 2017YFE0302400 and 2017YFA0402800), National Natural Science Foundation of China (Nos.: 11735015, 51871207, 11575229, U1832206) and Anhui Provincial Natural Science Foundation (No. 1908085J17). C.R.M. acknowledges the final support by the Brazilian Ministry of Science and Technology for collaborative researches between China and Brazil.

Appendix A. Supplementary data

Supplementary data to this article can be found online at https://doi.org/10.1016/j.jnucmat.2020.152223.

References

[1] I.J. Beyerlein, M.J. Demkowicz, A. Misra, B.P. Uberuaga, Defect-interface interactions, Prog. Mater. Sci. 74 (2015) 125–210.
[2] S. Lu, J. Ågren, L. Vitos, Ab initio study of energetics and structures of heterophase interfaces: from coherent to semicoherent interfaces, Acta Mater. 156 (2018) 20–30.
[3] W.-S. Jung, S.-H. Chung, Ab initio calculation of interfacial energies between transition metal carbides and fcc iron, Model. Simulat. Mater. Sci. Eng. 18 (2010), 075008.
[4] X.M. Bai, A.F. Voter, R.G. Hoagland, M. Nastasi, B.P. Uberuaga, Efficient annealing of radiation damage near grain boundaries via interstitial emission, Science 327 (2010) 1631–1634.
[5] D. Di Stefano, et al., First-principles investigation of hydrogen interaction with TiC precipitates in α-Fe, Phys. Rev. B 93 (2016) 184108.
[6] M. Rieth, et al., Review on the EFDA programme on tungsten materials technology and science, J. Nucl. Mater. 417 (2011) 463–467.
[7] S. Wurster, et al., Recent progress in R&D on tungsten alloys for divertor structural and plasma facing materials, J. Nucl. Mater. 442 (2013) S181–S189.
[8] C. Linsmeier, et al., Development of advanced high heat flux and plasma-facing materials, Nucl. Fusion 57 (2017), 092007.
[9] Z.M. Xie, et al., Extraordinary high ductility/strength of the interface designed bulk W-ZrC alloy plate at relatively low temperature, Sci. Rep. 5 (2015) 16014.
[10] H. Kurishita, et al., Development of ultra-fine grained W–(0.25–0.8)wt%TiC and its superior resistance to neutron and 3 MeV He-ion irradiations, J. Nucl. Mater. 377 (2008) 34–40.
[11] M. Miyamoto, et al., Observations of suppressed retention and blistering for tungsten exposed to deuterium-helium mixture plasmas, Nucl. Fusion 49 (2009), 065035.
[12] M. Zibrov, K. Bystrov, M. Mayer, T.W. Morgan, H. Kurishita, The high-flux effect on deuterium retention in TiC and TaC doped tungsten at high temperatures, J. Nucl. Mater. 494 (2017) 211–218.
[13] H. Kurishita, et al., Development of ultra-fine grained W–TiC and their mechanical properties for fusion applications, J. Nucl. Mater. 367–370 (2007) 1453–1457.
[14] F. Ishikawa, T. Takahashi, T. Ochi, Intragranular ferrite nucleation in medium-carbon vanadium steels, Metall. Mater. Trans. 25 (1994) 929–936.
[15] N.Y. Park, et al., First-principles study of the interfaces between Fe and transition metal carbides, J. Phys. Chem. C 117 (2013) 187–193.
[16] S.J. Zinkle, L.L. Snead, Designing radiation resistance in materials for fusion energy, Annu. Rev. Mater. Res. 44 (2014) 241–267.
[17] H. Kurishita, et al., Current status of nanostructured tungsten-based materials development, Phys. Scripta T159 (2014), 014032.
[18] Y. Mishin, M. Asta, J. Li, Atomistic modeling of interfaces and their impact on microstructure and properties, Acta Mater. 58 (2010) 1117–1151.
[19] C. González, R. Iglesias, M.J. Demkowicz, Point defect stability in a semicoherent metallic interface, Phys. Rev. B 91 (2015), 064103.
[20] M.A. Gibson, C.A. Schuh, Segregation-induced changes in grain boundary cohesion and embrittlement in binary alloys, Acta Mater. 95 (2015) 145–155.
[21] Z. Huang, F. Chen, Q. Shen, L. Zhang, T.J. Rupert, Combined effects of nonmetallic impurities and planned metallic dopants on grain boundary energy and strength, Acta Mater. 166 (2019) 113–125.
[22] G.B. Olson, Strong interface adhesion in Fe/TiC, Philos. Mag. A 85 (2005) 3683–3697.
[23] A. Arya, E.A. Carter, Structure, bonding, and adhesion at the ZrC(1 0 0)/Fe(1 1 0) interface from first principles, Surf. Sci. 560 (2004) 103–120.
[24] W.-S. Jung, S.-C. Lee, S.-H. Chung, Energetics for interfaces between group IV transition metal carbides and bcc iron, ISIJ Int. 48 (2008) 1280–1284.
[25] H. Sawada, S. Taniguchi, K. Kawakami, T. Ozaki, First-principles study of interface structure and energy of Fe/NbC, Model. Simulat. Mater. Sci. Eng. 21 (2013), 045012.
[26] D.Y. Dang, L.Y. Shi, J.L. Fan, H.R. Gong, First-principles study of W–TiC interface cohesion, Surf. Coating. Technol. 276 (2015) 602–605.
[27] J. Qian, C.Y. Wu, H.R. Gong, S.F. Zhou, Cohesion properties of W-ZrC interfaces from first principles calculation, J. Alloys Compd. 768 (2018) 387–391.
[28] X. Zhang, X. Wu, C. Hou, X. Li, C.S. Liu, First-principles calculations on interface stability and migration of H and He in W-ZrC interfaces, Appl. Surf. Sci. 499 (2020) 143995.
[29] G. Kresse, J. Hafner, Ab initio molecular dynamics for liquid metals, Phys. Rev. B 47 (1993) 558–561.
[30] G. Kresse, J. Furthmüller, Efficient iterative schemes for ab initio total-energy calculations using a plane-wave basis set, Phys. Rev. B 54 (1996) 11169–11186.
[31] P.E. Blöchl, Projector augmented-wave method, Phys. Rev. B 50 (1994) 17953–17979.
[32] J.P. Perdew, et al., Atoms, molecules, solids, and surfaces: applications of the generalized gradient approximation for exchange and correlation, Phys. Rev. B 46 (1992) 6671–6687.
[33] J.P. Perdew, et al., Erratum: atoms, molecules, solids, and surfaces: applications of the generalized gradient approximation for exchange and correlation, Phys. Rev. B 48 (1993), 4978-4978.
[34] K. Rasch, R. Siegel, H. Schultz, Quenching and recovery investigations of vacancies in tungsten, Philos. Mag. A 41 (1980) 91–117.
[35] H.-B. Zhou, Y.-L. Liu, Y. Zhang, S. Jin, G.-H. Lu, First-principles investigation of energetics and site preference of He in a W grain boundary, Nucl. Instrum. Methods Phys. Res., Sect. B 267 (2009) 3189–3192.
[36] W. Xu, A.P. Horsfield, D. Wearing, P.D. Lee, First-principles calculation of Mg/MgO interfacial free energies, J. Alloys Compd. 650 (2015) 228–238.
[37] M. Yamaguchi, M. Shiga, H. Kaburaki, Grain boundary decohesion by impurity segregation in a nickel-sulfur system, Science 307 (2005) 393–397.
[38] X. Wu, et al., First-principles determination of grain boundary strengthening in tungsten: dependence on grain boundary structure and metallic radius of solute, Acta Mater. 120 (2016) 315–326.
[39] S. Zhang, O.Y. Kontsevoi, A.J. Freeman, G.B. Olson, First principles investigation of zinc-induced embrittlement in an aluminum grain boundary, Acta Mater. 59 (2011) 6155–6167.
[40] J.H. Rose, J. Ferrante, J.R. Smith, Universal binding energy curves for metals and bimetallic interfaces, Phys. Rev. Lett. 47 (1981) 675.
[41] M. Acta MaterialiaZibrov, et al., Deuterium retention in TiC and TaC doped tungsten at high temperatures, J. Nucl. Mater. 463 (2015) 1045–1048.
[42] M. Zibrov, et al., Deuterium retention in TiC and TaC doped tungsten under low-energy ion irradiation, Phys. Scripta T159 (2014), 014050.
[43] R. Liu, et al., Recent progress on the R&D of W-ZrC alloys for plasma facing components in fusion devices, Nucl. Mater. Energy 16 (2018) 191–206.
[44] Z. Wu, X.-J. Chen, V.V. Struzhkin, R.E. Cohen, Trends in elasticity and electronic structure of transition-metal nitrides and carbides from first principles, Phys. Rev. B 71 (2005) 214103.
[45] X.-Y. Yang, Y. Lu, P. Zhang, First-principles study of the stability and diffusion properties of hydrogen in zirconium carbide, J. Nucl. Mater. 479 (2016) 130–136.
[46] X. Yang, Y. Lu, P. Zhang, First-principles study of native point defects and diffusion behaviors of helium in zirconium carbide, J. Nucl. Mater. 465 (2015) 161–166.
[47] X.-Y. Yang, Y. Lu, P. Zhang, The temperature-dependent diffusion coefficient of helium in zirconium carbide studied with first-principles calculations, J. Appl. Phys. 117 (2015) 164903.
[48] K. Darling, et al., Microstructure and mechanical properties of bulk nanostructured Cu–Ta alloys consolidated by equal channel angular extrusion, Acta Mater. 76 (2014) 168–185.
[49] K. Sasaki, K. Yabuuchi, S. Nogami, A. Hasegawa, Effects of temperature and strain rate on the tensile properties of potassium-doped tungsten, J. Nucl. Mater. 461 (2015) 357–364.
[50] X.-S. Kong, et al., First-principles calculations of hydrogen solution and diffusion in tungsten: temperature and defect-trapping effects, Acta Mater. 84 (2015) 426–435.
[51] X. Wu, et al., Effects of alloying and transmutation impurities on stability and mobility of helium in tungsten under a fusion environment, Nucl. Fusion 53 (2013), 073049.
[52] J. Takahashi, K. Kawakami, Y. Kobayashi, Origin of hydrogen trapping site in vanadium carbide precipitation strengthening steel, Acta Mater. 153 (2018) 193–204.

[53] R. Kirchheim, Changing the interfacial composition of carbide precipitates in metals and its effect on hydrogen trapping, Scripta Mater. 160 (2019) 62–65.
[54] X. Liu, et al., Irradiation effects of hydrogen and helium plasma on different grade tungsten materials, Nucl. Mater. Energy 12 (2017) 1314–1318.
[55] L. Yang, et al., The ferrite/oxide interface and helium management in nanostructured ferritic alloys from the first principles, Acta Mater. 103 (2016) 474–482.
[56] H. Kurishita, et al., Development of nanostructured tungsten based materials resistant to recrystallization and/or radiation induced embrittlement, Mater. Trans. 54 (2013) 456–465.
[57] B. AlMangour, M.-S. Baek, D. Grzesiak, K.-A. Lee, Strengthening of stainless steel by titanium carbide addition and grain refinement during selective laser melting, Mater. Sci. Eng., A 712 (2018) 812–818.